Dynamic CO2 separation performance of nanosized CHA zeolites under multi-component gas mixtures

Sajjad Ghojavand, Edwin Clatworthy, Benoit Coasne, Diógenes Honorato Piva, Rémy Guillet-Nicolas, Izabel Medeiris-Costa, Marie Desmurs, Valérie Ruaux, Veronique Pugnet, Parveen Kumar-Gandhi, et al.

Dynamic CO_2 separation performance of nano-sized CHA zeolites under multi-component gas mixtures

Sajjad Ghojavand[a*], Edwin B. Clatworthy[a], Benoit Coasne[b,c], Diógenes Honorato Piva[a], Rémy Guillet-Nicolas[a], Izabel C. Medeiris-Costa[c], Marie Desmurs[a], Valérie Ruaux[a], Veronique Pugnet[d], Parveen Kumar-Gandhi[d], Svetlana Mintova[a*]

[a] Normandie Université, ENSICAEN, UNICAEN, CNRS, Laboratoire Catalyse et Spectrochimie (LCS), 14000 Caen, France

[b] Université Grenoble Alpes, CNRS, Laboratoire Interdisciplinaire de Physique (LIPhy), 38000 Grenoble, France

[c] Institut Laue Langevin, F-38042 Grenoble, France

[d] TotalEnergies, OneTech, Sustainability R&D, CSTJF, 64018 Pau Cedex, France

Abstract:

To identify and evaluate promising adsorbents for CO_2 separation, we synthesized CHA zeolites with different cations (Na^+, K^+, Cs^+) and crystal sizes (45 nm – CHA45 and 500 nm – CHA500), and evaluated their explored CO_2 adsorption performance from CO_2/N_2/He and CO_2/CH_4/He mixtures. Grand Canonical Monte Carlo (GCMC) and molecular dynamics (MD) simulations predicted CO_2, N_2, and CH_4 adsorption isotherms and CO_2 mobilities, respectively, which were compared to experimental data. Breakthrough curve analysis was used to assess the CO_2 dynamic adsorption performance. The breakthrough curve analysis shows the smaller crystal sizes (45 nm) enhance the CO_2 separation due to shorter interacrystalline diffusion pathways. Notably, Cs-CHA45 removed 2.2 times more CO_2 from CO_2/N_2/He than Cs-CHA500. K-CHA45 showed the highest CO_2/N_2 selectivity (108) and achieved 841 mmol g^{-1} for CO_2 capture from N_2 and 721 mmol g^{-1} for CO_2 from CH_4. These findings underscore the potential of CHA nanocrystals for effective CO_2 separation in various applications.

Keywords: nanozeolite, chabazite, extra-framework cations, CO_2 adsorption, gas mixtures, separation, heat of adsorption

*Corresponding authors. E-mail addresses: sajjad.ghojavand@ensicaen.fr, +33231451330

svetlana.mintova@ensicaen.fr, +33231452737

1. Introduction

The growing concentration of atmospheric CO_2 is a matter of major global concern due to its far-reaching environmental ramifications such as climate change.[1,2] Strategies to address current and historic CO_2 emissions include reducing the use of carbon-based fuels, enhancing the energy efficiency of industrial sectors difficult to decarbonize, and the rapid transition to renewable energy.[2,3] In general, CO_2 capture should be considered as a last resort to avoid CO_2 emissions (1. avoid, 2. reduce, and 3. capture). However, with respect to CO_2 capture and separation, a triple procedural approach is necessary: (1) CO_2 capture/separation, (2) compression, and (3) sequestration or recycling, with the initial phase being particularly energy-intensive.[2–8] Among CO_2 capture and separation technologies, important examples include post-combustion capture, oxyfuel combustion, pre-combustion capture, and supercritical CO_2 cycles.[3,9–12] Presently, amine-based post-combustion capture is the most industrially mature technology for CO_2 capture.[13] While significant progress has been made to reduce the energy penalty associated with amine sorbent regeneration,[14] cost-effective and high-performance technologies still need to be developed and deployed. Consequently, the design of new materials with the ability to efficiently and sustainably separate CO_2 from other gases should be developed.[3,15–17] In this context, alternatives to amine solvents, including ionic liquids, membranes, and physical adsorbents, have received significant attention, with the latter constituting the focal point of this study.

High aluminum-containing zeolites, characterized by a Si/Al ratio < 3, have been the subject of significant research efforts due to their high CO_2 adsorption capacity and selectivity towards CO_2.[1,18,19] However, conventional zeolites, with particle sizes in the micrometer range, consist of aggregates of individual crystals which creates diffusion limitations of guest molecules within their pore networks.[20] This challenge can be effectively addressed by introducing mesoporosity, or by reducing the discrete zeolite particle size which reduces the internal diffusion pathway.[21] Nanozeolites, comprised of discrete particles or single crystals, exhibit a larger external surface area and a higher number of available active sites compared to their micron-sized counterparts.[22,23] To overcome the limitations mentioned above and benefit from the advantages of nanozeolites, we have developed protocols for synthesizing various zeolite structures with discrete nano-sized particles, utilizing exclusively inorganic cations (e.g., CHA, RHO, BPH, FAU, EMT, etc.) in our synthesis procedures.[1,18,19,24–29]

Zeolitic adsorbents are categorized by pore size into small (3.0–4.5 Å), medium (4.5–6 Å), large (6.0–8.0 Å), and extra-large (> 8.0 Å) pores.[30] Small-pore zeolites are particularly well-suited for CO_2 capture from mixtures containing N_2 or CH_4, as these molecules have similar kinetic diameters (3.3 Å for CO_2, 3.6 Å for N_2, and 3.8 Å for CH_4). A comprehensive review by Cheung and Hedin highlighted that, among small-pore zeolites, the CHA type zeolite exhibits the highest CO_2 adsorption capacities.[31] The accessibility of CHA's pore network, defined by its 8-membered rings (8MRs), can be modulated by extra-framework cations (EFCs) and adsorbed molecules, allowing for control over adsorption properties.[30,32–35] Two key mechanisms have been proposed for the selective adsorption of CO_2 on CHA zeolites: molecular sieving, which is based on the size difference between the pore openings and the kinetic diameters of gas molecules, and the molecular trapdoor mechanism, which arises from the structural flexibility of CHA imparted by EFCs.[1,34,36,37] The trapdoor mechanism occurs when EFCs occupy the 8MRs of the zeolite and regulate the access of guest molecules based on their interactions with these cations.[1,34,38] CO_2 molecules, in particular, can induce EFCs to move from the center of the 8MRs, allowing preferential entry of CO_2 into the CHA supercages while excluding non-polar gases like N_2 and CH_4.[34,35,38] These are the primary reasons we focus on CHA zeolite to separate CO_2 in the current study.

While numerous studies have examined the equilibrium adsorption of CO_2 on various alkali metal forms of CHA, there is a notable lack of comprehensive research on the dynamic CO_2 adsorption behavior of CHA zeolites under industrially relevant conditions, such as in multicomponent gas mixtures.[1,34,35,38] Previous work from our group has already demonstrated the potential of nano-sized Na-, K-, and Cs-CHA zeolites for CO_2 capture and separation.[1] In an earlier study, we found that when Na^+ cations dominate the CHA structure, the supercages remain open, allowing both CO_2 and N_2 molecules to enter, with CO_2 showing a high equilibrium capacity of 4.0 mmol g^{-1} at 298 K and 101 kPa.[1] However, when K^+ cations were the primary species, while CO_2 equilibrium capacity remained high (4.0 mmol g^{-1} under the same conditions), the micropore volume of CHA decreased significantly, indicating N_2 rejection.[1] A similar phenomenon was observed in the Cs-form of CHA.[1] Additionally, research by Shang *et al.* reported strong trapdoor behavior in the Cs^+ form of CHA, with CO_2/CH_4 selectivity exceeding 140 at 273 K.[34,35] These findings suggest that Na^+, K^+, and Cs^+ forms of CHA are highly promising for CO_2 capture and separation. As an initial step toward addressing the gaps in dynamic CO_2 adsorption studies on CHA, breakthrough curve analyses were conducted only on the K^+ form of nano-sized CHA (particle size ~60 nm) in comparison to its micron-sized counterpart (~1 μm), focusing on separating CO_2 from N_2.[39] This study revealed that nano-sized K-CHA exhibited a two-orders-of-magnitude higher effective mass transfer coefficient, or linear driving force parameter

(k_{LDF}), at 2.37 s^{-1} compared to 0.0221 s^{-1} for the micron-sized sample.[39] These results underscore the importance and need of conducting a detailed investigation into not only the equilibrium adsorption but also the dynamic behavior of CO_2 adsorption on Na^+, K^+, and Cs^+ forms of CHA under multicomponent gas mixtures, to better understand their potential for CO_2 separation from N_2 (flue gas) or CH_4 (natural gas).

To address this central issue, we synthesized six CHA zeolites with three different alkali metal compositions (Na^+, K^+, and Cs^+ cations) and two different crystal sizes (45 nm and 500 nm–an order of magnitude difference was selected to capture the effect of zeolite particle size and CO_2 diffusion limitations). We studied the dynamic CO_2 adsorption in multi-component gas mixtures of CO_2/N_2/He and CO_2/CH_4/He. Grand Canonical Monte Carlo (GCMC) calculations were also employed to predict the adsorption isotherms of CO_2, N_2, and CH_4. Additionally, molecular dynamics (MD) simulations were conducted to estimate CO_2 self-diffusivity in different alkali metal forms of CHA. The results were compared with experimentally obtained adsorption measurements. Finally, breakthrough curve analysis was used to investigate the CO_2 dynamic adsorption behavior from multi-component gas mixtures. Our findings indicate that CHA zeolites with smaller crystal sizes (45 nm) exhibit superior dynamic performance in separating CO_2 from N_2 or CH_4 due to the shorter diffusion pathways throughout the zeolite crystals. The results indicated that when comparing two CHA zeolite samples with particle sizes of 45 nm and 500 nm in their Na^+, K^+, and Cs^+ forms, the smaller particles exhibited significantly higher effective mass transfer coefficients (k_{LDF}). Specifically, the Na^+, K^+, and Cs^+ forms showed increases of one, two, and three orders of magnitude, respectively. Among these, nanosized K-CHA with a particle size of 45 nm demonstrated the highest CO_2 removal per month per adsorption column, achieving 841 mmol g^{-1} for CO_2/N_2 separation and 721 mmol g^{-1} for CO_2/CH_4 separation. It also exhibited the highest selectivity, with values of 108 for CO_2/N_2 and 78 for CO_2/CH_4. These results underscore the potential of CHA nanocrystals for CO_2 separation from N_2 or CH_4 in diverse applications.

2. Experimental and modeling section

2.1. Materials and synthesis of CHA nanocrystals

All reagents were used as received unless explicitly specified otherwise. Sodium hydroxide pellets (98 wt%), sodium chloride (99 wt%), potassium hydroxide (85 wt%), potassium chloride (99.5 wt%), LUDOX AS-40, and sodium aluminate ($NaAlO_2$, with 40–45% Na_2O and 50–56% Al_2O_3) were obtained from Sigma-Aldrich. Cesium hydroxide hydrate (99%, 15–20 wt% H_2O) and cesium chloride (99.5 wt%) were obtained from Alfa Aesar. Zeolite Y (H-form, CBV400) was purchased from

Zeolyst and used as a source for the preparation of CHA500 series of zeolite. Ultrapure Milli-Q water was employed for all synthesis steps.

2.1.1. Synthesis protocol of CHA45 series of zeolites

Nano-sized CHA zeolite (45 nm) was synthesized by upscaling our previously published protocol.[1] Initially, 10.80 g of $NaAlO_2$ was combined with 84.00 g of water under rapid stirring (350 rpm). Upon dissolution, 34.34 g of NaOH, 16.48 g of KOH, and 8.84 g of CsOH (50 wt.% Cs in water) were added and stirred for 2 hours to achieve a homogenous clear solution. Subsequently, 200 g of LUDOX AS-40 was added dropwise under vigorous stirring (500 rpm) to establish the initial gel composition of 0.2 Cs_2O: 1.5 K_2O: 6.0 Na_2O: 16.0 SiO_2: 0.7 Al_2O_3: 141.7 H_2O. The alkali metal aluminosilicate colloidal suspension underwent an aging process under vigorous stirring at room temperature for 17 days, followed by hydrothermal treatment in a static oven at 363 K for 7 hours. The resulting CHA nanocrystals were recovered by centrifugation, washed with hot water (363 K) until the decanted solution achieved a neutral pH (7–8), and subsequently dried in an oven at 333 K overnight. The final as-prepared CHA nanocrystals were designated as AP-CHA45. These nanocrystals underwent ion exchange with 1 M solutions of NaCl, KCl, and CsCl, each with a liquid/solid ratio (ml/g) of 40 for 2 hours. Following ion exchange, the CHA nanocrystals were recovered by centrifugation, washed with water three times, and this process was performed five times. The resulting nano-sized Na-, K-, and Cs-CHA45 were dried in an oven at 333 K overnight.

2.1.2. Synthesis protocol of CHA500 series of zeolites

CHA crystals with larger crystal sizes (500 nm) were synthesized following the procedure described by Shang *et al.*[34] Specifically, 25 g of zeolite Y powder was combined with 198 mL of water and 27 mL of a 9.5 M KOH solution. The mixture underwent shaking for one minute, and hydrothermal treatment was conducted at 368 K for 15 days. Subsequently, the crystals were recovered by centrifugation and washed with water until the decanted solution reached a neutral pH (7–8). The retrieved CHA crystals were then dried in an oven at 333 K overnight, and the final potassium-form was denoted as K-CHA500. The K-CHA500 zeolite underwent ion exchange with 1 M solutions of NaCl and CsCl, each with a liquid/solid ratio (ml/g) of 40 for 2 hours. Following ion exchange, CHA crystals were recovered by centrifugation and washed with water three times; this process was performed five times. The resulting zeolites were labelled Na- and Cs-CHA500, and dried in an oven at 333 K overnight. The precise chemical formulas of the different alkali metal forms of both CHA45 and CHA500 series were determined by ICP-MS provided in Table 1; note that AP-CHA45 zeolite is only used here to prepare Na-, K-, and Cs-CHA45 nano-sized zeolites and it is not mentioned further in the text, all characterizations regarding this sample are reported elsewhere.[1,29]

Table 1. Chemical composition of different alkali metal forms of CHA45 and CHA500 zeolites based on ICP-MS.

Sample	Chemical formula (ICP-MS)	Si/Al
AP-CHA45	$Na_{1.8}K_{5.7}Cs_{4.0}Al_{11.1}Si_{24.8}O_{72}$	2.2
Na-CHA45	$Na_{9.5}K_{0.5}Cs_{1.6}Al_{11.8}Si_{24.2}O_{72}$	2.1
K-CHA45	$K_{11.0}Cs_{0.8}Al_{11.7}Si_{24.2}O_{72}$	2.1
Cs-CHA45	$K_{1.6}Cs_{10.3}Al_{11.4}Si_{24.4}O_{72}$	2.1
Na-CHA500	$Na_{10.9}K_{0.8}Al_{12.3}Si_{23.9}O_{72}$	1.9
K-CHA500	$Na_{0.2}K_{12.8}Al_{12.4}Si_{23.5}O_{72}$	1.9
Cs-CHA500	$K_{2.3}Cs_{9.8}Al_{11.9}Si_{24.0}O_{72}$	2.0

2.2. Characterization techniques

Powder X-ray diffraction (PXRD) patterns were acquired using an Anton Paar XRDynamic 500 diffractometer with a graphitemonochromator in Bragg–Brentano configuration, Cu Kα_1 and Kα_2 radiation (λ = 1.5406, 1.5444 Å, 40 kV, 50 mA), and Pixos2000 detector. The patterns were collected between 2θ of 5° and 50° with a step size of 0.03° and time per step of 492.606 s. Inductively coupled plasma mass spectrometry (ICP-MS) measurements were conducted with an Agilent Technologies 7900 ICP-MS system.

Scanning Electron Microscopy (SEM) images were taken using a JEOL JSM-IT800 Schottky field emission scanning electron microscope in high-vacuum mode (pressure $<10^{-4}$ Pa) at a low accelerating voltage of 0.8 keV and a current of 10 nA. ImageJ software was used to analyze the particle size distribution according to the SEM images.

Adsorption isotherms for CO_2, N_2, and CH_4 were recorded at temperatures of 273 K, 298 K, and 313 K using a Micromeritics 3Flex Surface Characterization unit. The samples underwent an outgassing process under vacuum conditions at 623 K for a minimum of 7 hours prior to measurement. Isosteric heat of adsorption calculations for CO_2 were determined by applying the

Clausius-Clapeyron equation to CO_2 adsorption isotherms within the temperature range of 273 K to 313 K, utilizing the VersaWin software provided by Anton Paar.

Breakthrough curve experiments were conducted using a 3P Instruments mixSorb SHP eco in conjunction with a Cirrus-3 Quadrupole Mass Spectrometer. The zeolite adsorbent powder samples were initially pelletized by placing the powder between two core dies in a 20 mm die sleeve, with a base plate and plunger, and applying pressure until it reached approximately 1.5 tons. Subsequently, the pellets were gently crushed using a pestle and meshed from 60 to 35 (250–500 µm) before being loaded into the column, weighed, and covered with a thin layer of glass wool. Following the loading of meshed samples into the column, the column was tapped 100 times to eliminate inter-particle voids. The inner diameter of the column was 6 mm, and the height of the adsorbent bed was 6 cm, maintaining a column inner diameter to meshed particle diameter ratio of 12–24. The samples underwent pre-treatment under a helium (He) flow (20 mL min^{-1}) with heating from room temperature to 573 K at a rate of 10 K min^{-1} (measured by an internal temperature probe) and were held at 573 K for 7 hours using a heating mantle. Thermogravimetric analysis (TG) of the zeolite samples was carried out using a Setsys Evolution (SETARAM) under air, involving heating from room temperature to 573 K (heating rate of 10 K min^{-1}) and maintaining the temperature at 573 K for 7 hours to determine the water content evaporated during the activation step in the breakthrough analysis (Fig. S1). Following pre-treatment, the samples were exposed to a flow of He (20 mL min^{-1}) at room temperature before commencing the breakthrough curve experiments.

Breakthrough curve experiments were carried out using two ternary mixtures: CO_2/N_2 (analytical components)/He (carrier gas) and CO_2/CH_4/He, each at 1 bar with flow rates of 1.2, 6.0, and 12.8 mL min^{-1}, respectively, constituting a total flow of 20 mL min^{-1}. These flow rates correspond to 6%, 30%, and 64% of the feed composition, respectively, for the adsorption step. Prior to the breakthrough curve experiments, the mass spectrometer was calibrated by passing the ternary feed mixture through a bypass line to the mass spectrometer. Before coming into contact with the adsorbent column, the sample was subjected to a flow of He. The adsorption feed mixture was then directed through the adsorbent column after the temperature and spectrometer signals had stabilized, as determined using a bypass line. Following the establishment of equilibrium, desorption was initiated by switching the feed to 100% He (20 mL min^{-1}). Both the adsorption (until CO_2 breaks through ~60 min) and desorption steps (until CO_2 concentration is below $c/c_0 < 0.05$) were performed at 298 K. The pressure drop across the column loaded with the sample were determined by a pressure sensor located immediately before the column, and a pressure controller located immediately after the column. In all experiments conducted, the pressure drop was found to be less than 0.07 bar or 6% of the column pressure. Helium is treated as a non-adsorbing gas

within the system. The dead-time of the system was approximated to be ≈2 s, determined by considering the time of activation of the mass-flow controllers and recording the flow composition by the mass spectrometer through the bypass line.

All breakthrough curve data was processed using the mixSorb Manager software. The competitive and effective loadings of the adsorbates (CO_2, N_2, and CH_4) were calculated from the integrated areas exemplified in Fig. S2 and Fig. S3. To obtain CO_2 loadings, the adsorption branch of the breakthrough curves was used (Fig. S2a,b). To avoid the uncertainties on estimating the N_2 and CH_4 loadings based on the adsorption branch of the breakthrough curves due to the roll-up effect (Fig. S2c,d), the desorption branch of the breakthrough was used to estimate these loadings (Fig. S3).

$$n_{adsorbed} = \int V_{in}(t)c_{in}(t)dt - \int V_{out}(t)c_{out}(t)dt \quad (1)$$

where $n_{adsorbed}$ is the amount of molecule adsorbed, V_{in} is the volume of the column inlet, V_{out} is the volume of the column outlet, c_{in} is the concentration at column inlet, and c_{out} is the concentration at column outlet.

$$V_{out}(t) = \frac{V_{He}(t)}{1 - \sum_{i=1}^{n} y_{adsorptive,i}(t)} \quad (2)$$

where V_{He} is the volume of He and $y_{adsorptive}$ is the adsorptive volume fraction.

To determine the loading of molecules in the free space between adsorbent particles, blank experiments were conducted using granular quartz under identical conditions of feed composition, temperature, flow rate, and pressure. These values were then directly subtracted from the loading values of the zeolite samples (Fig. S4).

Fig. S5 and Fig. S6 show the breakthrough curves and their corresponding temperature profiles versus time for two gas mixtures of CO_2/N_2/He and CO_2/CH_4/He (6/30/64) on different CHA45 and CHA500 zeolite samples. In all cases, the temperature changes inside the adsorption column is small (< 0.25 K).

All isotherm and CO_2 breakthrough curve modelling was performed using the 3P-Sim software package (see Supporting Information). The experimental CO_2 adsorption isotherms were fitted with a temperature dependent model. LAI, Sips, and Toth models were employed.[40] The model with the best goodness of fit was selected for specific zeolites (Table S5). These models were then employed for the CO_2 breakthrough curve modelling.

The CO_2/N_2 and CO_2/CH_4 selectivities were calculated using equation (3) based on predicted adsorption isotherms, experimentally measured isotherms, and competitive dynamic adsorption experiments.

$$\frac{CO_2}{x}(selectivity) = \left(\frac{q_{CO_2}}{n_{CO_2}}\right) / \left(\frac{q_x}{n_x}\right) \quad (3)$$

where *q* is the loading of adsorbate, *n* is the molar amount of adsorbate in the feed, and *x* is N_2 or CH_4.

2.3. Grand Canonical Monte Carlo calculations and molecular dynamics simulations

We employed our previously established CHA supercell, comprising 27 CHA unit cells, as the basis for all Grand Canonical Monte Carlo (GCMC) calculations.[1] Force field parameters were adopted from the work of Jeffroy and co-workers.[41] Partial charges for Si, Al, and O in the zeolite were adjusted to +1.384, +1.190, and –0.831, respectively, following the methodology outlined by Mortier and co-workers.[42] The interaction parameters for CO_2, N_2, and CH_4 were obtained from the comprehensive study conducted by Wu and co-workers.[43] GCMC simulations were conducted for CO_2, N_2, and CH_4 adsorption at 298 K in CHA zeolite samples containing various alkali metal cations. The simulations were performed in accordance with the chemical compositions determined through ICP-MS analysis of nano-sized CHA samples (refer to Table 1). The GCMC technique, a stochastic method, was employed to simulate a system with a constant volume *V* (representing the pore with the adsorbed phase), in equilibrium with an infinite reservoir of particles imposing their chemical potential μ_{CO2} for the adsorbed species and temperature *T*. The absolute adsorption isotherm is determined by the ensemble average of the number of each adsorbate molecule as a function of the CO_2 fugacity (f_{CO2}) of the reservoir, with the latter determined from the chemical potential μ.

Molecular Dynamics (MD) simulations were conducted in the classical limit, employing a force field based on parameters developed by Gabrieli and co-workers.[44] This force field, tailored for zeolites and already applied to LTA, FAU, and MFI structures, accommodates the flexibility of zeolite structures during simulations.[44] The MD simulations were carried out on different alkali metal forms of CHA for two CO_2 doses (32 and 196 molecules in 27 CHA unit cells) and two structural modes (rigid and flexible). To validate the results, additional MD simulations were performed on an all-silica CHA model (designated as Si-CHA) for two CO_2 doses (32 and 196 molecules in 27 CHA unit cells) and two structural modes (rigid and flexible). The self-diffusivities of CO_2, denoted as $D_{CO2,self}$, were computed by analyzing the mean square displacement of CO_2 molecules using equation (4):

$$D_{CO_2,self} = \frac{1}{2N_i} \lim_{\Delta t \to \infty} \frac{1}{\Delta t} \left\langle \left(\sum_{l=1}^{N_i} \left(r_{l,i}(t + \Delta t) - r_{l,t}(t) \right)^2 \right) \right\rangle \qquad (4)$$

where, N_i represents the number of CO_2 molecules, and $r_{l,i}(t)$ denotes the position of the *i*th CO_2 molecule at any given time *t*. The average values in the three coordinate directions are then reported. All simulations were conducted for a duration of 100 ns. In fact, it was found that despite such a long simulation time the Fickian regime is not reached *i.e.* $\Delta r^2(t) \sim t$. Consequently, we

note that *stricto sensu* the transport coefficient $D_{CO_2,self}$ as defined in Eq. (1) should be referred to as mobility rather than self-diffusivity. Therefore, for the sake of rigor, throughout this manuscript, $D_{CO_2,self}$ will be coined as mobility to avoid confusion but the overall discussion will remain unchanged.

All calculation/simulation resulted from GCMC and MD methods abbreviated as Na-CHA-M, K-CHA-M, Cs-CHA-M, and Si-CHA-M (for an all silica forms of CHA to validate the simulations with literature).

3. Results and discussion

Two sets of CHA zeolites with different extra-framework cation compositions (Na^+, K^+, and Cs^+) and different crystal sizes were prepared. The exact chemical compositions of the different samples are reported in Table 1. The zeolitic phase of the different alkali metal forms of the CHA zeolites was verified by PXRD, (Fig. S7) and are consistent with our previous studies and the literature. For the nano-sized Na-CHA45 zeolite only, a small impurity of phillipsite phase at 12.5° 2θ resulted due to the upscaling the synthesis protocol; however, the overall bulk adsorption behavior of this zeolite sample is unchanged (*vide infra*).[1,29,34,45] The crystal size and particle morphologies of the alkali metal forms of CHA zeolites were characterized using SEM analysis (Fig. 1). The CHA45 samples are comprised of discrete CHA crystals with an average size of 45 nm, whereas the CHA500 samples feature flake-like particles with an average size of 500 nm, composed of aggregated crystals (Fig. 1).

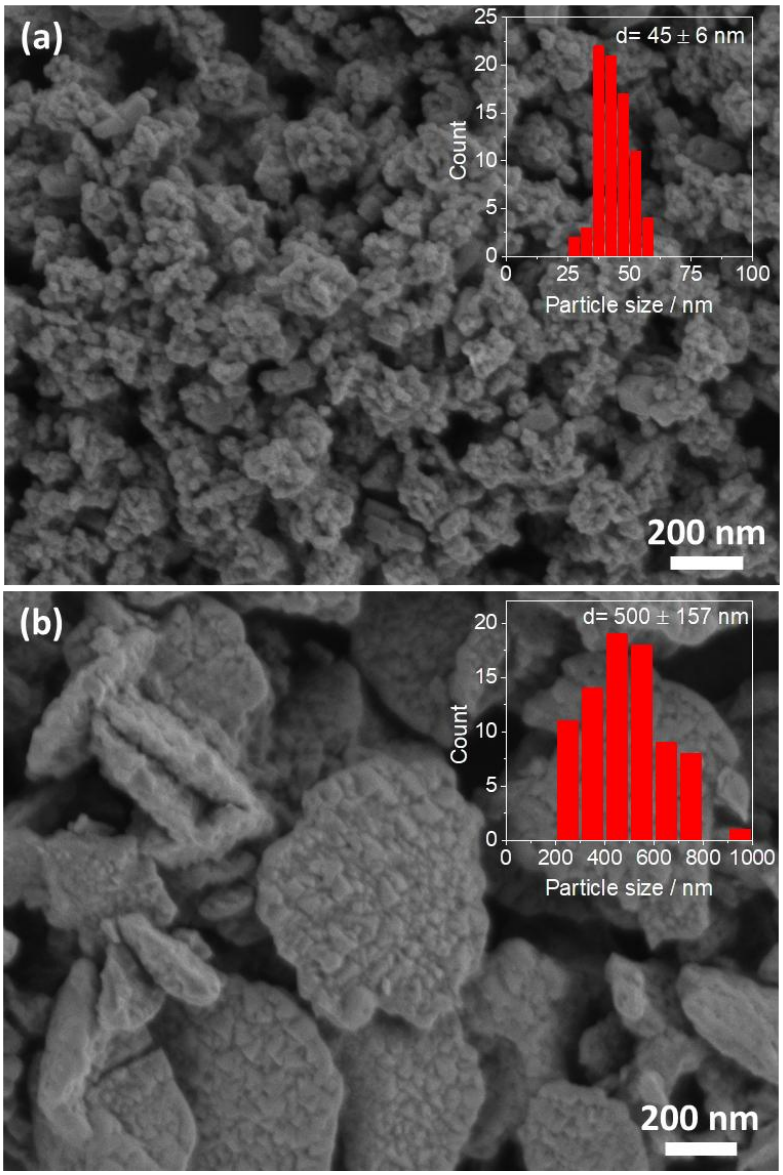

Fig. 1. SEM images of (a) K-CHA45 and (b) K-CHA500 and their corresponding particle size distributions (inset) as examples of two series (CHA45 and CHA500) of zeolites.

The adsorption isotherms of CO_2, N_2, and CH_4 on the CHA samples were initially predicted using the GCMC method for different alkali metal forms of CHA zeolite at 298 K (Fig. 2). Fig. 2 indicates that the capacities of guest molecules (CO_2, N_2, and CH_4) decrease with increasing size of the extra-framework cations. This trend is expected, as less free volume is available inside the CHA framework, which aligns with previous findings.[1,34,46]

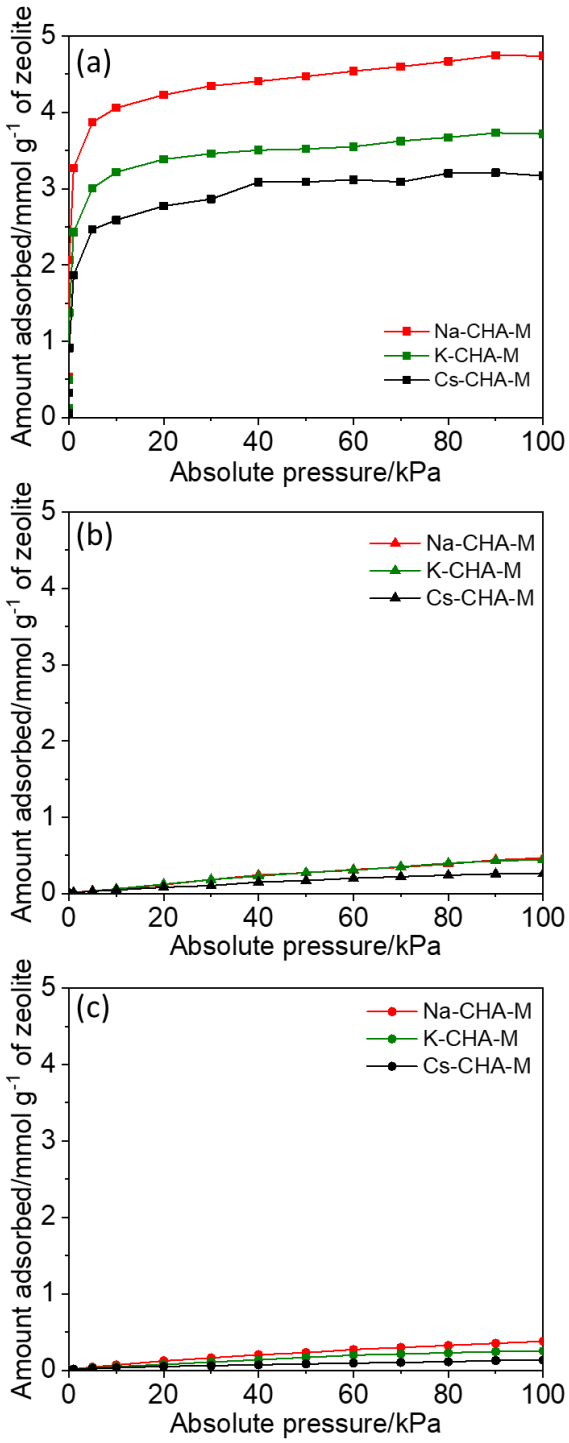

Fig. 2. (a) CO_2, (b) N_2, and (c) CH_4 adsorption isotherms of Na-CHA-M, K-CHA-M, and Cs-CHA-M zeolites at 298 K calculated using the GCMC method.

Table 2 presents the predicted CO_2 capacities at 6 kPa, and N_2 and CH_4 capacities at 30 kPa, estimated using the GCMC method of single-component adsorption isotherms for different alkali metal forms of CHA at 298 K. The CO_2/N_2 and CO_2/CH_4 ideal selectivities were also predicted (this is consistent with our breakthrough curve analysis gas composition and intended for comparison with the dynamic results, *vide infra*) and are presented in Table 2. In contrast to the guest-molecule

capacities, the predicted CO_2/N_2 selectivities increase slightly across the different alkali metal forms of CHA, while the CO_2/CH_4 selectivities increase more strongly with the size of the extra-framework cations. This trend may be influenced by the decrease of the charge density of the alkali metal cations as their size increases, and the concomitant increase of the zeolite framework oxygen basicity as the interaction of the quadrupole moments of CO_2 molecules with the zeolite framework (including the extra-framework cations) are the dominant interactions. Depending on the precise arrangement of the guest molecule within the zeolite microporosity, larger cations may preferentially interact with more polarizable molecules such as CO_2 compared to N_2 or CH_4. This general trend aligns with observations made by Shang *et al.* in their study of micron-sized Li-, Na-, K-, Rb-, and Cs-CHA zeolites.[35] In addition, K^+ and Cs^+ cations were found to occupy the main entrances of the CHA pores (eight-membered rings, 8MR), leading to the trapdoor effect.[1,34,35,38] This behavior allows for the selective admittance of CO_2 molecules while rejecting neutral gas species such as N_2 and CH_4.[1,34,35,38] This phenomenon is further supported by the ideal selectivity predicted by GCMC, as shown in Table 2.

Table 2. Predicted equilibrium loadings of CO_2, N_2, and CH_4 at 298 K, the predicted ideal selectivity of CO_2/N_2 and CO_2/CH_4 at 298 K, and CO_2 mobility at low and high loadings at 600 K inside the flexible structural mode of Na-CHA-M, K-CHA-M, and Cs-CHA-M zeolites were calculated using the GCMC method and molecular dynamics simulations.

Sample	**Predicted equilibrium loading at 298 K/ mmol g^{-1}**			**Selectivity at 298 K**		**CO_2 mobility/ m^2 s^{-1}**	
	CO_2 (6 kPa)	**N_2 (30 kPa)**	**CH_4 (30 kPa)**	**CO_2/N_2[a]**	**CO_2/CH_4[a]**	**Low loading[b]**	**High loading[c]**
Na-CHA-M	3.92	0.185	0.164	106	120	8.1×10^{-13}	12.0×10^{-13}
K-CHA-M	3.07	0.141	0.107	109	143	4.2×10^{-13}	6.7×10^{-13}
Cs-CHA-M	2.50	0.105	0.062	119	202	2.8×10^{-13}	3.6×10^{-13}
Si-CHA-M	-	-	-	-	-	6.6×10^{-9}	7.0×10^{-9}

[a]at 6 Kpa CO_2 and 30 kPa N_2 or CH_4
[b]32 CO_2 molecules in 27 CHA unit cells
[c]196 CO_2 molecules in 27 CHA unit cells

Fig. 3 and Fig. S8, along with Table 2 and Table S1, present the mean-squared displacement of CO_2 molecules *vs.* time and their corresponding CO_2 mobility within different alkali metal forms of CHA zeolite at two temperatures (298 K and 600 K), considering two CO_2 loadings (low and high: 32 and 196 CO_2 molecules in 27 CHA unit cells, respectively), and two structural modes (rigid *vs.* flexible) calculated using MD simulations. To validate the MD results, an all-silica CHA (Si-CHA) was also simulated, given that CO_2 mobility MD simulations are commonly performed on all-silica zeolite types in the literature.[47–50] This validation, as depicted in Table 2 and Table S1, reveals that the CO_2 mobility on Si-CHA under different conditions falls within the range of $2–7\times10^{-9}$ m^2

s^{-1}, consistent with the findings of Krishna and co-workers (2×10^{-9} m^2 s^{-1}).[47] In contrast, as already discussed, for CO_2 in CHA with cations, the Fickian regime could not be reached so that we only discuss the corresponding mobility. Based on the results presented in Table 2 and Fig. S9, it can be concluded that the calculated CO_2 mobilities are inversely proportional to the size of the extra-framework cations. When comparing the CO_2 mean-square displacements of CO_2 in the different alkali metal forms of CHA to those of Si-CHA zeolite, the values decrease by several orders of magnitudes. This indicates that the CO_2 adsorption sites in the various alkali metal forms of CHA are significantly stronger than those in all-silica CHA zeolite, indicative of their potential for CO_2 capture and storage using these zeolites.

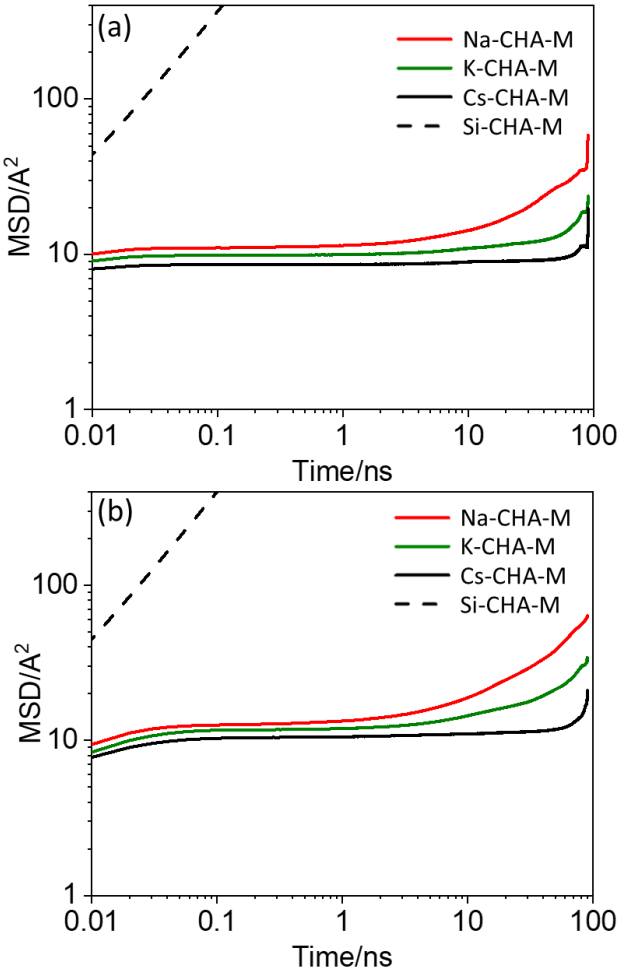

Fig. 3. Mean-squared displacement of CO_2 molecules over time at 600 K for (a) low CO_2 loading (32 molecules in 27 unit cell) and (b) high CO_2 loading (196 molecules in 27 unit cell) at 600 K and flexible zeolite structural mode.

Experimentally, both the CHA45 and CHA500 sample series were analyzed for CO_2, N_2, and CH_4 adsorption at 273 K, 298 K, and 313 K, with the results presented in Fig. 4, Fig. S10, and Fig.

S11. Equilibrium loadings of CO_2, N_2, and CH_4 at 298 K and the ideal selectivity for CO_2/N_2 and CO_2/CH_4 (for a gas mixture of CO_2/N_2 or CO_2/CH_4 at 6/30 kPa) for various alkali metal forms of CHA zeolites are shown in Table 3 and Table S2. Fig. 4, Fig. S10, and Fig. S11 indicate that the equilibrium loadings of guest molecules decrease as the temperature increases from 273 K to 313 K, due to the exothermic nature of the adsorption process.[1,39]

Fig. S12 illustrates the isosteric heat of adsorption (HOA) of CO_2 on different alkali metal forms of zeolites from series CHA45 and CHA500, ranging from 30 to 60 kJ mol^{-1} depending on CO_2 loading and CHA composition, consistent with previous findings.[1,39,51] The higher CO_2 HOA values for the CHA45 and CHA500 sets (30–65 kJ mol^{-1}) compared to all-silica CHA zeolite (20 kJ mol^{-1}) indicate a greater affinity for CO_2 molecules in the CHA45 and CHA500 sets.[52] These findings correspond with the lower CO_2 mobilities calculated for various alkali metal forms of CHA using MD simulations (Table 2).

The experimentally determined equilibrium loadings of guest molecules (Table 3 and Table S4) are inversely proportional to the size of the extra-framework cations, which is consistent with our GCMC predictions (Table 2) and the literature.[1,34,35] With a constant Si/Al ratio (∼2.0) across all CHA samples, the use of smaller extra-framework cations (*e.g.*, Na^+) results in more available space within the CHA unit cell, providing more space for guest molecules. Comparing the GCMC-predicted isotherms (Fig. 2) with experimentally measured isotherms (Fig. 4) for the series CHA45 nanosized zeolites at 298 K shows overall agreement, although GCMC predictions tend to overestimate equilibrium loadings (Table 2 *vs* Table 3). This overestimation is particularly evident for CO_2 equilibrium loadings of Cs-CHA-M, predicted by GCMC, compared to experimentally measured nano-sized Cs-CHA45 zeolite at 6 kPa and 298 K (2.50 *vs.* 0.57 mmol g^{-1}, Table 2 *vs.* Table 3). The experimentally measured CO_2 equilibrium loadings of the different alkali metal forms of nano-sized CHA45 presented in Table 3, along with our previous work[1] and the work of Shang *et al.*[35], indicate that the Cs^+ content significantly restricts CO_2 access to the adsorption sites within CHA cages. However, the GCMC method does not account for these diffusion limitations. Supporting this, the CO_2 adsorption isotherms for Na-CHA500 and K-CHA500 (Fig. S11b) align perfectly with GCMC-predicted isotherms for Na-CHA-M and K-CHA-M at 298 K (Fig. 2). Conversely, the experimentally measured CO_2 isotherms for Cs-CHA500 (Fig. S11b) compared to GCMC predictions for Cs-CHA-M at 298 K (Fig. 2) show a clear overestimation of CO_2 capacities by GCMC. While Na-CHA500 and K-CHA500 CO_2 capacities at 298 K match GCMC predictions (Fig. S11b *vs.* Fig. 2), overestimation remains for nanosized Na-CHA45 and K-CHA45 zeolite samples (Fig. 2 *vs*. Fig. 4). As already mentioned, this discrepancy arises because GCMC predictions assume perfect zeolite crystals with ideal extra-framework cation compositions, comparable to the compositions of Na-CHA500 and K-CHA500 presented in Table 1. However, some Cs^+ cations remain in the Na-CHA45

and K-CHA45 samples (1.6 and 0.8 Cs^+ per unit cell, respectively – Table 1), which cannot be exchanged due to the role of Cs^+ stabilizing the nanosized CHA zeolites.[29] Consequently, the presence of Cs^+ cations leads to an overestimation of guest-molecule capacities in Na-CHA45 and K-CHA45 zeolites. One possible solution to improve the accuracy of GCMC predictions is to block specific regions of the CHA unit cell where CO_2 molecules are unable to diffuse. However, this requires a separate investigation to precisely locate the cations and define their mobility window, which can then be used to restrict CO_2 adsorption.

When comparing the predicted N_2 adsorption isotherm for K-CHA-M (Fig. 2b) with the experimentally measured isotherm for K-CHA45 (Fig. 4b) at 298 K, an overestimation of N_2 uptake is evident in the GCMC-predicted isotherms. This discrepancy can be attributed to the presence of trace amounts of Cs^+ cations (0.8 Cs^+ per unit cell – see Table 1) in nanosized K-CHA45 zeolite. Similarly, when comparing the predicted CH_4 adsorption isotherms for various alkali metal forms of CHA (Na-, K-, Cs-CHA-M) using GCMC (Fig. 2c) with the experimentally measured isotherms of the CHA45 series (Na-, K-, Cs-CHA45) (Fig. 4c) at 298 K, an underestimation is observed across all CH_4 predictions. This suggests that the force field parameters for CH_4 may require refinement to enhance the accuracy of these predictions, particularly in the context of CH_4 interactions with high-aluminum-content zeolites, as is the case in this study. However, this falls beyond the scope of the present work and warrants its own dedicated investigation.

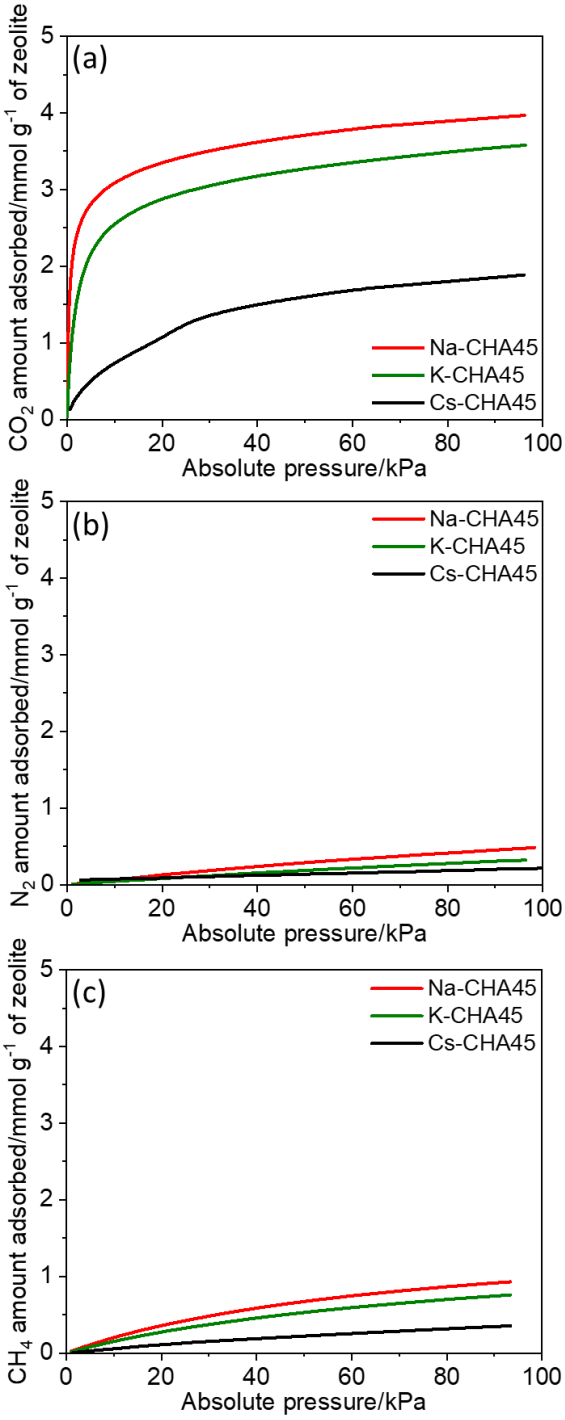

Fig. 4. (a) CO_2, (b) N_2, and (c) CH_4 adsorption isotherms of nano-sized Na-CHA45, K-CHA45, and Cs-CHA45 zeolites at 298 K.

The highest ideal selectivity for both CO_2/N_2 and CO_2/CH_4 at equilibrium is observed in K-CHA45 zeolite, following the order K-CHA45 > Na-CHA45 > Cs-CHA45 (Table 3). This contrasts with the GCMC predictions presented in Table 2, where the selectivity for both CO_2/N_2 and CO_2/CH_4 is proportional to the size of the extra-framework cations. The discrepancy in CO_2/CH_4 ideal selectivity between Na-CHA45, Na-CHA500, K-CHA45, and K-CHA500 compared to the GCMC predictions, is mainly due to the underestimation of CH_4 adsorption isotherms. This suggests that

the force field parameters for CH_4 may need refinement for more accurate predictions. Additionally, the overestimation of both CO_2/N_2 and CO_2/CH_4 predicted selectivity for Cs-CHA-M zeolite using GCMC is attributed to the diffusion barriers of CO_2 molecules and the overestimation of CO_2 adsorption isotherms, as previously discussed (*vide supra*).

Table 3. Equilibrium loadings of CO_2, N_2, and CH_4 based on single-component adsorption isotherms at 6, 30, and 30 kPa, respectively for different alkali metal forms of nano-sized series CHA45 zeolites. CO_2/N_2 and CO_2/CH_4 experimental ideal selectivity is calculated for a CO_2/N_2 or CO_2/CH_4 mixture of 6/30 based on equation (3).

Sample	**Equilibrium loading at 298 K/ mmol g^{-1}**			**Ideal selectivity at 298 K**	
	CO_2 (6 kPa)	**N_2 (30 kPa)**	**CH_4 (30 kPa)**	**CO_2/N_2**	**CO_2/CH_4**
Na-CHA45	2.90	0.184	0.482	79	30
K-CHA45	2.28	0.116	0.373	98	31
Cs-CHA45	0.57	0.105	0.152	63	19

The single-cycle adsorption and desorption breakthrough curves for two gas mixtures, CO_2/N_2/He and CO_2/CH_4/He (6/30/64), for different alkali metal forms of nano-sized CHA45 zeolites are depicted in Fig. 5 and Fig. S13. Similarly, Fig. S14 shows single-cycle adsorption and desorption breakthrough curves for the same gas mixtures with series CHA500 zeolites. Comparing Fig. 5a, b and Fig. S14a,b, it is evident that the CO_2 breakthrough curves for all alkali metal forms of the nano-sized CHA45 are steeper, regardless of the co-adsorbents (N_2 or CH_4), compared to their CHA500 counterparts, where a diffusion profile is visible along the adsorption bed. This observation is consistent with our previous report comparing K-CHA nano-sized and micron-sized zeolites.[39] The faster sorption kinetics of the nano-sized CHA45 zeolites are also apparent in the desorption branches of the breakthrough curves (Fig. 5c,d and Fig. S13 *vs.* Fig. S14c,d,e,f).

The time required to achieve CO_2 desorption ($C/C_0 < 0.05$) under pure He flow decreases significantly with increasing size of the extra-framework cations (Na^+ to Cs^+) as shown in Fig. 5c,d and Fig. S14c,d. The normalized CO_2 desorption times for Na-CHA45, K-CHA45, and Cs-CHA45 for the CO_2/N_2/He mixture are 213, 117, and 27 min g^{-1}, respectively, and for the CO_2/CH_4/He mixture, they are 210, 131, and 24 min g^{-1}, respectively (Table 4).

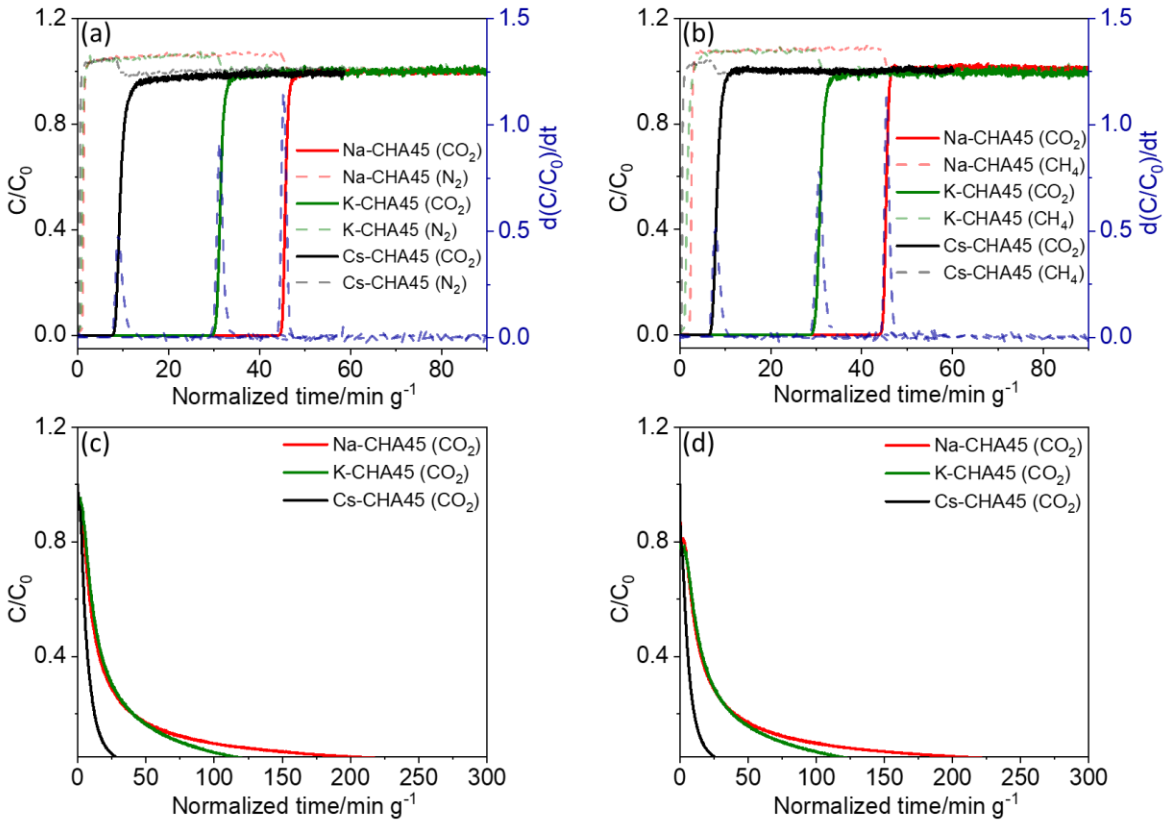

Fig. 5. (a) and (b) CO_2 and N_2 adsorption branches of breakthrough curves for gas mixtures of CO_2/N_2/He and CO_2/CH_4/He (6/30/64), respectively, for different alkali metal forms of nano-sized series CHA45 zeolites at 298 K. (c) and (d) CO_2 desorption branches of breakthrough curves for the same gas mixtures and zeolites at 298 K.

Table 4 and Table S3 present CO_2, N_2, and CH_4 competitive equilibrium loadings, CO_2 normalized desorption times, and competitive CO_2/N_2 and CO_2/CH_4 selectivities at equilibrium for the different alkali metal forms of the two series zeolites CHA45 and CHA500 under multi-component gas mixtures of CO_2/N_2/He and CO_2/CH_4/He. Comparing the CO_2, N_2, and CH_4 loadings from breakthrough measurements under multi-component gas mixtures with equilibrium adsorption under single-component gases (Table 4 and Table 3), a slight reduction in CO_2 loadings is observed for different alkali metal forms of nanosized CHA45 zeolites. For example, CO_2 loadings resulted from breakthrough and isotherm measurements are 2.43 mmol g^{-1} compared to 2.90 mmol g^{-1} for Na-CHA45, and 1.93 mmol g^{-1} compared to 2.28 mmol g^{-1} for K-CHA45, respectively. This reduction is due to the competitive adsorption of N_2 or CH_4 with CO_2, leading to fewer available adsorption sites for CO_2 molecules and also it could be due to the timeframe and kinetics of the experiments. During equilibrium adsorption analysis, there is enough time to reach equilibrium thermodynamically. In comparison, during dynamic adsorption, the diffusion/adsorption kinetics also competes against the CO_2 gas flow rate. This behavior is also observed in different alkali metal forms of CHA500 zeolites, as presented in Table S3. Similar

reductions in CO_2 loadings when using mixed-component gas mixtures versus single-component gases were noted in our previous work on K-CHA nano-sized zeolites (1.49 *vs.* 1.61 mmol g^{-1} at 313 K).[39]

Regarding CO_2/N_2 and CO_2/CH_4 competitive selectivity at equilibrium, the highest selectivity is observed for K-CHA45 (CO_2/N_2 = 108 and CO_2/CH_4 = 78, Table 4). This trend is consistent with the ideal selectivity results presented in Table 3; the trend K-CHA45 > Na-CHA45 > Cs-CHA45 based on equilibrium adsorption measurements is confirmed.

Table 4. Competitive equilibrium loadings of CO_2, N_2, and CH_4 based on multi-component breakthrough measurements for different alkali metal forms of nano-sized CHA45 zeolites. CO_2/N_2 and CO_2/CH_4 competitive selectivity is calculated for gas mixtures of CO_2/N_2/He or CO_2/CH_4/He (6/30/64) based on equation (2).

Sample	**Competitive equilibrium loading at 298 K/ mmol g^{-1}**				**CO_2 normalized desorption time/ min g^{-1}**		**Competitive selectivity**	
	CO_2/N_2/He		**CO_2/CH_4/He**		**CO_2/N_2/He**	**CO_2/CH_4/He**	**CO_2/N_2**	**CO_2/CH_4**
	CO_2	**N_2**	**CO_2**	**CH_4**				
Na-CHA45	2.43	0.229	2.48	0.187	213	210	53	66
K-CHA45	1.93	0.089	1.69	0.108	117	131	108	78
Cs-CHA45	0.54	0.060	0.42	0.096	27	24	45	22

CO_2 loadings presented in Table 4 and Table S3 (labelled as "competitive loadings") are estimated when the adsorption bed reached equilibrium. However, for industrial applications, CO_2 loadings at equilibrium are less relevant since the primary goal is to continuously capture and separate CO_2 from the inlet stream using the adsorption column, avoiding CO_2 presence in the outlet streams. Considering a maximum permitted outlet CO_2 concentration of $C/C_0 < 0.05$, a new parameter, "effective CO_2 loading," was introduced and illustrated in Fig. 6 and Fig. S15 using Cs-CHA45 and Cs-CHA500 zeolites as examples. Fig. 6a shows the area of the breakthrough curves corresponding to the competitive CO_2 loadings presented in Table 4 and Table S3; for Cs-CHA45, it is 0.54 mmol g^{-1}, and for Cs-CHA500, it is 0.50 mmol g^{-1}. This is consistent with the adsorption isotherms presented in Table 3 and Table S2. Both Cs-CHA45 and Cs-CHA500 samples show similar CO_2 capacities at equilibrium, which is expected since their chemical compositions are very similar (Table 1). Thus, at equilibrium, they should present the same CO_2 capacities. The main difference between these samples is their discrete crystal sizes (45 *vs.* 500 nm).

Larger discrete crystal sizes lead to longer diffusion pathways and slower kinetics to reach equilibrium, which is evident in Fig. 6 when comparing the CO_2 breakthrough curves of Cs-CHA45 versus Cs-CHA500. For Cs-CHA500, the diffusion front within the adsorption bed reaches the outlet after approximately 2 minutes of CO_2 adsorption, and the bed reaches equilibrium after 25

minutes. However, in the case of Cs-CHA45, the diffusion front reaches the outlet significantly later, after 8 minutes, and the adsorption bed reaches equilibrium within 5 minutes only (Fig. 6). More uniform CO_2 diffusion through Cs-CHA45 compared to Cs-CHA500 means the adsorption bed can be used more efficiently. This is clearly illustrated in Fig. 6b, where considering a limiting permitted CO_2 concentration of $C/C_0 < 0.05$ in the outlet stream, the areas corresponding to the effective CO_2 loading for Cs-CHA45 are significantly higher than those for Cs-CHA500. The same behavior regarding the diffusion front was observed when separating CO_2 from a mixture containing CO_2/CH_4/He (6/30/64), as shown in Fig. S15.

Table 5 and Table S4 present the effective CO_2 loadings, CO_2 cycle duration, and estimated possible CO_2 removal per month using different alkali metal forms of CHA45 and CHA500 zeolites for gas mixtures of CO_2/N_2/He and CO_2/CH_4/He (6/30/64) at 298 K, respectively. Comparing the results summarized in Table 5 and Table S4, the effective CO_2 loading of Cs-CHA45 is 2.5 times greater than that of Cs-CHA500 (0.46 vs. 0.18 mmol g^{-1}) when separating CO_2 from N_2. Additionally, the time required to desorb CO_2 in Cs-CHA45 is 15% shorter than that for Cs-CHA500 (27 *vs.* 32 min g^{-1}). These findings suggest that CO_2 cycling is more efficient with smaller crystals. Consequently, the possible amount of CO_2 that can be separated in a single adsorption column over one month was estimated (Table 5 and Table S4). The amount of CO_2 that can be removed in one month from a mixture of CO_2/N_2/He (6/30/64) using Cs-CHA45 is 2.2 times greater than that using Cs-CHA500 (523 *vs.* 236 mmol g^{-1} – Table 5 *vs.* Table S4).

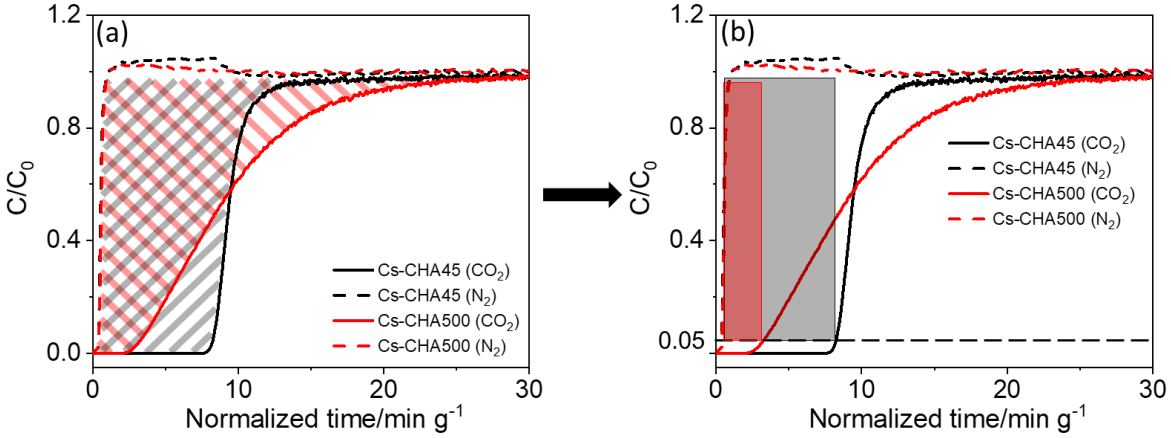

Fig. 6. (a) CO_2 and N_2 breakthrough curves for the gas mixture of CO_2/N_2/He (6/30/64) where CO_2 competitive loadings at equilibrium are highlighted by grey lines for nanosized Cs-CHA45 and by red lines for Cs-CHA500 at 298 K, and (b) highlighting the effective CO_2 loadings for $C/C_0 < 0.05$ by the grey shaded area for Cs-CHA45 and red shaded area for Cs-CHA500 at 298 K.

Based on the data presented in Table 5 and Table S4, the K-CHA45 and K-CHA500 zeolites exhibit the highest monthly CO_2 removal efficiency when using a single adsorption column,

irrespective of the stream composition (CO_2/N_2/He or CO_2/CH_4/He). Additionally, as indicated in Table 4 and Table S3, these zeolites also demonstrate good CO_2/N_2 and CO_2/CH_4 selectivity. The enhanced CO_2 separation performance of K-CHA zeolites, compared to their Na- or Cs-CHA counterparts, can be attributed to two interrelated factors: 1) CO_2 capacities, and 2) charge density of the extra-framework cations. Moving up the period from Cs to Na, the diameter of the respective cations decreases significantly, thereby creating more space within the CHA unit cell to accommodate additional CO_2 molecules, leading to increased CO_2 capacities (refer to Table 3, Table 4, Table 5, Table S2, Table S3, and Table S4). However, since Na^+, K^+, and Cs^+ cations are all monovalent, a reduction in cationic diameter corresponds to an increase in cation charge density, resulting in stronger interactions with the quadrupole moments of CO_2 molecules. Consequently, CO_2 regeneration demands more energy and time, as evidenced by the longer CO_2 desorption times (Table 4 and Table S3) and extended CO_2 cycle durations (Table 5 and Table S4), including when normalized to the adsorbed amount of CO_2. Therefore, a trade-off exists, wherein various K-forms of CHA zeolite exhibit the best CO_2 separation performance.

Conversely, the nano-sized K-CHA45 zeolites exhibit superior diffusion properties compared to K-CHA500, resulting in the highest monthly CO_2 removal rates. Specifically, K-CHA45 achieves 841 mmol g^{-1} for CO_2 capture from N_2 and 721 mmol g^{-1} for CO_2 removal from CH_4 (Table 5). Additionally, these zeolites demonstrate the highest CO_2/N_2 and CO_2/CH_4 selectivity, with values of 108 and 78, respectively (Table 4 and Table S3). As a consequence, the nano-sized K-CHA45 zeolite presents the best CO_2 separation performance, making it a promising candidate for CO_2 capture and separation applications.

Table 5. Effective CO_2 loadings, CO_2 cycle duration, and estimated possible CO_2 removed per month based on multi-component breakthrough measurements for the gas mixture of CO_2/N_2/He (6/30/64) for different alkali metal forms of nano-sized CHA zeolites at 298 K.

Sample	**Effective CO_2 loading at 298 K/ mmol g^{-1}**		**CO_2 cycle duration* / min**		**CO_2 removed per month** / mmol g^{-1}**	
	CO_2/N_2/He	**CO_2/CH_4/He**	**CO_2/N_2/He**	**CO_2/CH_4/He**	**CO_2/N_2/He**	**CO_2/CH_4/He**
Na-CHA45	2.46	2.46	161	164	660	648
K-CHA45	1.85	1.62	95	97	841	721
Cs-CHA45	0.46	0.39	38	34	523	496

*Cycle duration = breakthrough time ($C/C_0 < 0.05$) + CO_2 desorption time ($C/C_0 < 0.05$)
**CO_2 removed per month = 43200 (duration of a month/min) / cycle duration × effective CO_2 loading

The modeling of CO_2 breakthrough curves was conducted to determine the effective mass transfer coefficient, or linear driving force parameter (k_{LDF}), which characterizes the mass transfer behavior of CO_2 through the adsorbent bed. Table S5 details all the parameters utilized in modeling

the CO_2 breakthrough curves. Fig. S16 and Fig. S17 display the experimentally measured and fitted CO_2 breakthrough curves for $CO_2/N_2/He$ and $CO_2/CH_4/He$ mixtures, respectively, for various alkali metal forms of CHA45 and CHA500 zeolites. Table 6 presents the k_{LDF} parameters obtained from modeling the CO_2 breakthrough curves for different alkali metal forms of series CHA45 and CHA500 zeolites with gas mixtures of $CO_2/N_2/He$ and $CO_2/CH_4/He$.

According to Table 6, when comparing the CHA45 and CHA500 sets of zeolites, significantly higher k_{LDF} values are observed for the different alkali metal forms of nanosized CHA45 zeolites. Specifically, Na-CHA45 exhibits k_{LDF} values an order of magnitude higher than Na-CHA500. K-CHA45 demonstrates k_{LDF} values two orders of magnitude higher than K-CHA500, consistent with our previous work.[39] Finally, Cs-CHA45 shows the greatest difference, with k_{LDF} values three orders of magnitude higher than Cs-CHA500. These results further support our previous conclusions towards superior diffusion kinetics within different alkali metal forms of nanosized CHA45 zeolites.

Table 6. Calculated linear driving force parameters (k_{LDF}) obtained from the modelling of the CO_2 breakthrough curves for different alkali metal forms of CHA45 and CHA500 at 298 K.

Sample	k_{LDF} / min^{-1}	
	$CO_2/N_2/He$	**$CO_2/CH_4/He$**
Na-CHA45	120.8	108.8
Na-CHA500	17.2	11.6
K-CHA45	114.4	114.4
K-CHA500	1.3	1.1
Cs-CHA45	126.4	138.4
Cs-CHA500	0.4	0.4

The type and content of alkali metal cations (Na^+, K^+, or Cs^+), as well as the size of the CHA crystals, significantly influence the CO_2 capture performance of CHA zeolites in separating CO_2 from N_2 or CH_4. An interesting observation is that the effect of changing the extra-framework cation appears to be associated with a greater relative change of the k_{LDF} values for the micron-sized CHA zeolites. In contrast, the k_{LDF} values for the nano-sized CHA zeolites are of all the same order of magnitude. This behavior is clearly visible by comparing the slopes of the breakthrough curves. This indicates that at the nanoscale, the extra-framework cation chemistry becomes less important with respect to the mass-transfer behavior, yet is strongly influential for the overall adsorption capacity. GCMC method serves as a robust tool for predicting the adsorption behavior of CHA zeolites and potentially other solid adsorbents with varying compositions, temperatures, and guest molecules. This method offers an initial screening to identify optimal adsorbents for CO_2 separation applications. However, it is crucial to consider diffusion limitations within the porous structure of

the adsorbents. Our study demonstrates that diffusion limitations can lead to increased guest-molecule capacity predictions with the addition of larger Cs^+ cations, as evidenced by comparing the results presented in Fig. 2 with Fig. 4, that are consistent with our previous findings.[1] A comprehensive equilibrium adsorption study on different alkali metal forms of CHA45 and CHA500 zeolites reveals that guest-molecule capacities are inversely proportional to the size of the extra-framework cations, aligning with GCMC simulations (Fig. 2, Fig. 4, Fig. S10, Fig. S11, Table 3, and Table S2).[1,34,35] MD simulations indicate that the CO_2 self-diffusivities in various alkali metal forms of CHA are four orders of magnitude lower than those in all-silica CHA zeolites (Table 2 and Table S1). This suggests that these CHA forms have strong adsorption sites for CO_2, as reflected in the high CO_2 isosteric HOA observed in both CHA45 and CHA500 sets (Fig. S12), corroborating literature reports.[1,39,51] Due to the strong affinity of different alkali metal forms of CHA zeolite towards CO_2 molecules, both CHA45 and CHA500 sets exhibit selectivity for CO_2 separation from N_2 or CH_4, as demonstrated by breakthrough measurement studies (Fig. 5, Fig. S14, Table 4, and Table S3). This study highlights that, in addition to cationic composition, the size of the CHA zeolite crystals is a crucial parameter for CO_2 separation. This is illustrated by the instantaneous CO_2 breakthrough of Cs-CHA45 (mean crystal size of 45 nm) compared to Cs-CHA500 (mean crystal size of 500 nm) shown in Fig. 6. This observation is further supported by the calculated linear driving force (k_{LDF}) of CO_2 breakthrough curves, which are 1–3 orders of magnitude higher for the different alkali metal forms of nano-sized CHA45 compared to the CHA500 sets. Further analysis of breakthrough curves under two gas mixtures (CO_2/N_2/He or CO_2/CH_4/He) presented in Fig. 5 and Fig. S14, indicates that nano-sized K-CHA45 zeolites, due to the optimal charge density of K^+ cations, exhibit the highest CO_2 effective capacities (1.85 mmol g^{-1} for CO_2 separation from N_2 and 1.62 mmol g^{-1} for CO_2 separation from CH_4 – Table 5) and CO_2/N_2 and CO_2/CH_4 selectivities of 108 and 78, respectively (Table 4). Therefore, nano-sized K-CHA45 zeolite emerges as the most promising candidate for CO_2 capture and separation applications amongst the alkali metal CHA zeolites. Further studies are necessary to explore the effects of zeolite shaping and to conduct process engineering simulations for designing feasible adsorption operation units. Specifically, to explore the proposed cyclic CO_2 loadings in a real industrial setting (shaped zeolites with binders and appropriate CO_2 regeneration based on specific industrial capabilities) for real-world scenarios (*i.e.* utilizing nanosized K-CHA45 zeolite as future adsorbent for CO_2 capture and separation).

4. Conclusions

A comprehensive equilibrium and dynamic adsorption study of CO_2, N_2, and CH_4 on different alkali metal forms of chabazite (CHA) zeolites (Na-, K-, and Cs-forms) with two distinct nanosized crystal sizes was conducted. These included the nano-sized CHA45 series (crystal size of 45 nm) and

the CHA500 series (crystal size of 500 nm). Initially, adsorption isotherms were predicted using Grand Canonical Monte Carlo (GCMC) calculations. Experimental adsorption isotherms for CO_2, N_2, and CH_4 were measured at 248, 273, and 298 K. Finally, the adsorption dynamics were investigated using breakthrough curve analysis at 298 K for two ternary gas mixtures, $CO_2/N_2/He$ and $CO_2/CH_4/He$ (6/30/64 vol%). GCMC predictions, along with equilibrium and dynamic adsorption results, indicate that CO_2 capacities for nanosized CHA45 and CHA500 are inversely proportional to the size of the alkali metal cations (Na-CHA > K-CHA > Cs-CHA). The GCMC method is a robust tool for predicting the adsorption behavior of CHA zeolites and potentially other solid adsorbents with varying compositions, temperatures, and guest molecules, providing an initial screening to identify optimal adsorbents for CO_2 separation applications. Based on breakthrough curve analysis, nano-sized CHA45 zeolites exhibit a steeper CO_2 breakthrough and faster CO_2 desorption compared to CHA500 zeolites. For example, estimating the amount of CO_2 that can be separated over one month using a single adsorption column, more than 120% improvement in CO_2 removal is observed for Cs-CHA45 compared to Cs-CHA500, due to the faster diffusion kinetics through the smaller discrete zeolite crystals. Hence, synthesizing zeolites (and possibly other porous adsorbents) with nano-sized dimensions is crucial for enhancing diffusion throughout the porous material. Among different alkali metal forms of the nanosized CHA45, K-CHA45 demonstrates the highest CO_2 removal per month per adsorption column (841 for CO_2/N_2 separation and 721 mmol g^{-1} for CO_2/CH_4 separation) and selectivity (CO_2/N_2 = 108 and CO_2/CH_4 = 78). Therefore, nano-sized K-CHA45 zeolite emerges as a promising candidate for CO_2 capture and separation applications.

Authors contribution

S. G.: synthesis, analysis, validation, visualization, conceptualization, writing of original draft, review & editing; E. D.: validation, writing – review & editing; B. C.: validation, funding acquisition, writing – review & editing; D. P.: validation, writing – review & editing; R.G.: validation, writing – review & editing; I. M.: validation; M. D.: analysis; V. R.: analysis, V. P.: validation, writing – review & editing; P. K.: validation; S. M.: validation, project administration, resources, funding acquisition, writing – review & editing.

Conflicts of interest

The authors declare that they have no known competing financial interests or personal relationships that could have appeared to influence the work reported in this paper.

Acknowledgement

The support of the Centre for Zeolites and Nanoporous Materials, Label of Excellence, Normandy Region (CLEAR) and Eco-Gas Indistrial Chair TotalEnergies is acknowledged. Co-funded by the European Union (ERC, ZEOLIghT, 101054004). Views and opinions expressed are however those of the author(s) only and do not necessarily reflect those of the European Union or the European Research Council. Neither the European Union nor the granting authority can be held responsible for them. Numerical simulations were performed using the Froggy platform of the GRICAD infrastructure (https://gricad.univ-grenoble-alpes.fr), which is supported by the Rhone-Alpes Region (grant CPER07-13 CIRA) and the Equip@Meso Project (reference 10-EQPX-29-01) of the programme Investissements d'Avenir supervised by the French National Research Agency.

5. References

[1] S. Ghojavand, B. Coasne, E.B. Clatworthy, R. Guillet-Nicolas, P. Bazin, M. Desmurs, L. Jacobo Aguilera, V. Ruaux, S. Mintova, Alkali Metal Cations Influence the CO2 Adsorption Capacity of Nanosized Chabazite: Modeling vs Experiment, ACS Appl. Nano Mater. 5 (2022) 5578–5588. https://doi.org/10.1021/acsanm.2c00537.

[2] L.C. Tomé, I.M. Marrucho, Ionic liquid-based materials: a platform to design engineered CO_2 separation membranes, Chem. Soc. Rev. 45 (2016) 2785–2824. https://doi.org/10.1039/C5CS00510H.

[3] M.-A. Pizzoccaro, Confinement and grafting of ionic liquids in mesoporous ceramic membranes for the selective transport of CO2, thesis, Montpellier, 2017. http://www.theses.fr/2017MONTS007 (accessed November 16, 2018).

[4] M.G. Cowan, D.L. Gin, R.D. Noble, Poly(ionic liquid)/Ionic Liquid Ion-Gels with High "Free" Ionic Liquid Content: Platform Membrane Materials for CO_2 /Light Gas Separations, Acc. Chem. Res. 49 (2016) 724–732. https://doi.org/10.1021/acs.accounts.5b00547.

[5] Y.-S. Bae, R.Q. Snurr, Development and Evaluation of Porous Materials for Carbon Dioxide Separation and Capture, Angew. Chem. Int. Ed. 50 (2011) 11586–11596. https://doi.org/10.1002/anie.201101891.

[6] A. Samanta, A. Zhao, G.K.H. Shimizu, P. Sarkar, R. Gupta, Post-Combustion CO2 Capture Using Solid Sorbents: A Review, Ind. Eng. Chem. Res. 51 (2012) 1438–1463. https://doi.org/10.1021/ie200686q.

[7] B. Li, Y. Duan, D. Luebke, B. Morreale, Advances in CO2 capture technology: A patent review, Appl. Energy 102 (2013) 1439–1447. https://doi.org/10.1016/j.apenergy.2012.09.009.

[8] D.Y.C. Leung, G. Caramanna, M.M. Maroto-Valer, An overview of current status of carbon dioxide capture and storage technologies, Renew. Sustain. Energy Rev. 39 (2014) 426–443. https://doi.org/10.1016/j.rser.2014.07.093.

[9] M. Pera-Titus, Porous Inorganic Membranes for CO2 Capture: Present and Prospects, Chem. Rev. 114 (2014) 1413–1492. https://doi.org/10.1021/cr400237k.

[10] P.A. Webley, Adsorption technology for CO2 separation and capture: a perspective, Adsorption 20 (2014) 225–231. https://doi.org/10.1007/s10450-014-9603-2.

[11] N. Gargiulo, F. Pepe, D. Caputo, CO2 Adsorption by Functionalized Nanoporous Materials: A Review, J. Nanosci. Nanotechnol. 14 (2014) 1811–1822. https://doi.org/10.1166/jnn.2014.8893.

[12] S.-Y. Lee, S.-J. Park, A review on solid adsorbents for carbon dioxide capture, J. Ind. Eng. Chem. 23 (2015) 1–11. https://doi.org/10.1016/j.jiec.2014.09.001.

[13] S.E. Zanco, J.-F. Pérez-Calvo, A. Gasós, B. Cordiano, V. Becattini, M. Mazzotti, Postcombustion CO2 Capture: A Comparative Techno-Economic Assessment of Three Technologies Using a Solvent, an Adsorbent, and a Membrane, ACS Eng. Au 1 (2021) 50–72. https://doi.org/10.1021/acsengineeringau.1c00002.
[14] A. Hamidian, R. Bonnart, M. Lacroix, V. Moreau, A Pilot Plant in Dunkirk for DMX Process Demonstration, (2021). https://doi.org/10.2139/ssrn.3821422.
[15] Z. Zhang, T.N. Borhani, A.G. Olabi, Status and perspective of CO2 absorption process, Energy 205 (2020) 118057. https://doi.org/10.1016/j.energy.2020.118057.
[16] F. Raganati, F. Miccio, P. Ammendola, Adsorption of Carbon Dioxide for Post-combustion Capture: A Review, Energy Fuels 35 (2021) 12845–12868. https://doi.org/10.1021/acs.energyfuels.1c01618.
[17] R.L. Siegelman, E.J. Kim, J.R. Long, Porous materials for carbon dioxide separations, Nat. Mater. 20 (2021) 1060–1072. https://doi.org/10.1038/s41563-021-01054-8.
[18] J. Grand, N. Barrier, M. Debost, E.B. Clatworthy, F. Laine, P. Boullay, N. Nesterenko, J.-P. Dath, J.-P. Gilson, S. Mintova, Flexible Template-Free RHO Nanosized Zeolite for Selective CO2 Adsorption, Chem. Mater. 32 (2020) 5985–5993. https://doi.org/10.1021/acs.chemmater.0c01016.
[19] E.B. Clatworthy, M. Debost, N. Barrier, S. Gascoin, P. Boullay, A. Vicente, J.-P. Gilson, J.-P. Dath, N. Nesterenko, S. Mintova, Room-Temperature Synthesis of BPH Zeolite Nanosheets Free of Organic Template with Enhanced Stability for Gas Separations, ACS Appl. Nano Mater. 4 (2021) 24–28. https://doi.org/10.1021/acsanm.0c02925.
[20] L. Tosheva, V.P. Valtchev, Nanozeolites: Synthesis, Crystallization Mechanism, and Applications, Chem. Mater. 17 (2005) 2494–2513. https://doi.org/10.1021/cm047908z.
[21] S. Mintova, J. Grand, V. Valtchev, Nanosized zeolites: Quo Vadis?, Comptes Rendus Chim. 19 (2016) 183–191. https://doi.org/10.1016/j.crci.2015.11.005.
[22] S. Mintova, J.-P. Gilson, V. Valtchev, Advances in nanosized zeolites, Nanoscale 5 (2013) 6693–6703. https://doi.org/10.1039/C3NR01629C.
[23] G.-T. Vuong, T.-O. Do, Nanozeolites and Nanoporous Zeolitic Composites: Synthesis and Applications, in: Mesoporous Zeolites, John Wiley & Sons, Ltd, 2015: pp. 79–114. https://doi.org/10.1002/9783527673957.ch3.
[24] E.-P. Ng, D. Chateigner, T. Bein, V. Valtchev, S. Mintova, Capturing Ultrasmall EMT Zeolite from Template-Free Systems, Science 335 (2012) 70–73. https://doi.org/10.1126/science.1214798.
[25] H. Awala, J.-P. Gilson, R. Retoux, P. Boullay, J.-M. Goupil, V. Valtchev, S. Mintova, Template-free nanosized faujasite-type zeolites, Nat. Mater. 14 (2015) 447–451. https://doi.org/10.1038/nmat4173.
[26] M. Debost, P.B. Klar, N. Barrier, E.B. Clatworthy, J. Grand, F. Laine, P. Brázda, L. Palatinus, N. Nesterenko, P. Boullay, S. Mintova, Synthesis of Discrete CHA Zeolite Nanocrystals without Organic Templates for Selective CO2 Capture, Angew. Chem. 132 (2020) 23697–23701. https://doi.org/10.1002/ange.202009397.
[27] E.B. Clatworthy, A.A. Paecklar, E. Dib, M. Debost, N. Barrier, P. Boullay, J.-P. Gilson, N. Nesterenko, S. Mintova, Engineering RHO Nanozeolite: Controlling the Particle Morphology, Al and Cation Content, Stability, and Flexibility, ACS Appl. Energy Mater. 5 (2022) 6032–6042. https://doi.org/10.1021/acsaem.2c00439.
[28] M. Debost, E.B. Clatworthy, J. Grand, N. Barrier, N. Nesterenko, J.-P. Gilson, P. Boullay, S. Mintova, Direct synthesis of nanosized CHA zeolite free of organic template by a combination of cations as structure directing agents, Microporous Mesoporous Mater. (2022) 112337. https://doi.org/10.1016/j.micromeso.2022.112337.
[29] S. Ghojavand, E.B. Clatworthy, A. Vicente, E. Dib, V. Ruaux, M. Debost, J. El Fallah, S. Mintova, The role of mixed alkali metal cations on the formation of nanosized CHA zeolite from colloidal precursor suspension, J. Colloid Interface Sci. 604 (2021) 350–357. https://doi.org/10.1016/j.jcis.2021.06.176.
[30] M. Dusselier, M.E. Davis, Small-Pore Zeolites: Synthesis and Catalysis, Chem. Rev. 118 (2018) 5265–5329. https://doi.org/10.1021/acs.chemrev.7b00738.

[31] O. Cheung, N. Hedin, Zeolites and related sorbents with narrow pores for CO2 separation from flue gas, RSC Adv. 4 (2014) 14480–14494. https://doi.org/10.1039/C3RA48052F.
[32] M.M. Lozinska, E. Mangano, A.G. Greenaway, R. Fletcher, S.P. Thompson, C.A. Murray, S. Brandani, P.A. Wright, Cation Control of Molecular Sieving by Flexible Li-Containing Zeolite Rho, J. Phys. Chem. C 120 (2016) 19652–19662. https://doi.org/10.1021/acs.jpcc.6b04837.
[33] V.M. Georgieva, E.L. Bruce, M.C. Verbraeken, A.R. Scott, W.J. Casteel, S. Brandani, P.A. Wright, Triggered Gate Opening and Breathing Effects during Selective CO2 Adsorption by Merlinoite Zeolite, J. Am. Chem. Soc. 141 (2019) 12744–12759. https://doi.org/10.1021/jacs.9b05539.
[34] J. Shang, G. Li, R. Singh, Q. Gu, K.M. Nairn, T.J. Bastow, N. Medhekar, C.M. Doherty, A.J. Hill, J.Z. Liu, P.A. Webley, Discriminative Separation of Gases by a “Molecular Trapdoor” Mechanism in Chabazite Zeolites, J. Am. Chem. Soc. 134 (2012) 19246–19253. https://doi.org/10.1021/ja309274y.
[35] J. Shang, G. Li, R. Singh, P. Xiao, J.Z. Liu, P.A. Webley, Determination of Composition Range for “Molecular Trapdoor” Effect in Chabazite Zeolite, J. Phys. Chem. C 117 (2013) 12841–12847. https://doi.org/10.1021/jp4015146.
[36] M.M. Lozinska, E. Mangano, J.P.S. Mowat, A.M. Shepherd, R.F. Howe, S.P. Thompson, J.E. Parker, S. Brandani, P.A. Wright, Understanding Carbon Dioxide Adsorption on Univalent Cation Forms of the Flexible Zeolite Rho at Conditions Relevant to Carbon Capture from Flue Gases, J. Am. Chem. Soc. 134 (2012) 17628–17642. https://doi.org/10.1021/ja3070864.
[37] S. Ghojavand, E. Dib, S. Mintova, Flexibility in zeolites: origin, limits, and evaluation, Chem. Sci. 14 (2023) 12430–12446. https://doi.org/10.1039/D3SC03934J.
[38] G. (Kevin) Li, J. Shang, Q. Gu, R.V. Awati, N. Jensen, A. Grant, X. Zhang, D.S. Sholl, J.Z. Liu, P.A. Webley, E.F. May, Temperature-regulated guest admission and release in microporous materials, Nat. Commun. 8 (2017) 1–9. https://doi.org/10.1038/ncomms15777.
[39] E.B. Clatworthy, S. Ghojavand, R. Guillet-Nicolas, J.-P. Gilson, P.L. Llewellyn, N. Nesterenko, S. Mintova, Dynamic Adsorption of CO2 by CHA Zeolites – Size Matters, Chem. Eng. J. (2023) 144557. https://doi.org/10.1016/j.cej.2023.144557.
[40] M.A. Al-Ghouti, D.A. Da’ana, Guidelines for the use and interpretation of adsorption isotherm models: A review, J. Hazard. Mater. 393 (2020) 122383. https://doi.org/10.1016/j.jhazmat.2020.122383.
[41] M. Jeffroy, A. Boutin, A.H. Fuchs, Understanding the Equilibrium Ion Exchange Properties in Faujasite Zeolite from Monte Carlo Simulations, J. Phys. Chem. B 115 (2011) 15059–15066. https://doi.org/10.1021/jp209067n.
[42] L. Uytterhoeven, D. Dompas, W.J. Mortier, Theoretical investigations on the interaction of benzene with faujasite, J. Chem. Soc. Faraday Trans. 88 (1992) 2753–2760. https://doi.org/10.1039/FT9928802753.
[43] X. Wu, J. Huang, W. Cai, M. Jaroniec, Force field for ZIF-8 flexible frameworks: atomistic simulation of adsorption, diffusion of pure gases as CH4, H2, CO2 and N2, RSC Adv. 4 (2014) 16503–16511. https://doi.org/10.1039/C4RA00664J.
[44] A. Gabrieli, M. Sant, P. Demontis, G.B. Suffritti, Development and Optimization of a New Force Field for Flexible Aluminosilicates, Enabling Fast Molecular Dynamics Simulations on Parallel Architectures, J. Phys. Chem. C 117 (2013) 503–509. https://doi.org/10.1021/jp311411b.
[45] M. Bourgogne, J.-L. Guth, R. Wey, Process for the preparation of synthetic zeolites, and zeolites obtained by said process, US4503024A, 1985. https://patents.google.com/patent/US4503024/en (accessed November 12, 2021).
[46] S. Ghojavand, E. Dib, J. Rey, A. Daouli, E.B. Clatworthy, P. Bazin, V. Ruaux, M. Badawi, S. Mintova, Interplay between alkali-metal cations and silanol sites in nanosized CHA zeolite and implications for CO2 adsorption, Commun. Chem. 6 (2023) 1–8. https://doi.org/10.1038/s42004-023-00918-1.

[47] R. Krishna, J.M. van Baten, E. García-Pérez, S. Calero, Diffusion of CH4 and CO2 in MFI, CHA and DDR zeolites, Chem. Phys. Lett. 429 (2006) 219–224. https://doi.org/10.1016/j.cplett.2006.08.015.
[48] S.E. Jee, D.S. Sholl, Carbon Dioxide and Methane Transport in DDR Zeolite: Insights from Molecular Simulations into Carbon Dioxide Separations in Small Pore Zeolites, J. Am. Chem. Soc. 131 (2009) 7896–7904. https://doi.org/10.1021/ja901483e.
[49] S. Jost, P. Biswas, A. Schüring, J. Kärger, P.A. Bopp, R. Haberlandt, S. Fritzsche, Structure and Self-Diffusion of Water Molecules in Chabazite: A Molecular Dynamics Study, J. Phys. Chem. C 111 (2007) 14707–14712. https://doi.org/10.1021/jp073857s.
[50] D. Dubbeldam, E. Beerdsen, S. Calero, B. Smit, Dynamically Corrected Transition State Theory Calculations of Self-Diffusion in Anisotropic Nanoporous Materials, J. Phys. Chem. B 110 (2006) 3164–3172. https://doi.org/10.1021/jp0542470.
[51] T.D. Pham, M.R. Hudson, C.M. Brown, R.F. Lobo, Molecular Basis for the High CO2 Adsorption Capacity of Chabazite Zeolites, ChemSusChem 7 (2014) 3031–3038. https://doi.org/10.1002/cssc.201402555.
[52] H. Maghsoudi, M. Soltanieh, H. Bozorgzadeh, A. Mohamadalizadeh, Adsorption isotherms and ideal selectivities of hydrogen sulfide and carbon dioxide over methane for the Si-CHA zeolite: comparison of carbon dioxide and methane adsorption with the all-silica DD3R zeolite, Adsorption 19 (2013) 1045–1053. https://doi.org/10.1007/s10450-013-9528-1.